

pubs.acs.org/JPCC Article

Interface-Mediated Resonant Raman Enhancement for Shear Modes in a 2D Polar Metal

Published as part of The Journal of Physical Chemistry virtual special issue "Cynthia Friend Festschrift". Wen He, Maxwell T. Wetherington, Kanchan Ajit Ulman, Joshua A. Robinson, and Su Ying Quek*



Cite This: J. Phys. Chem. C 2022, 126, 14581-14589



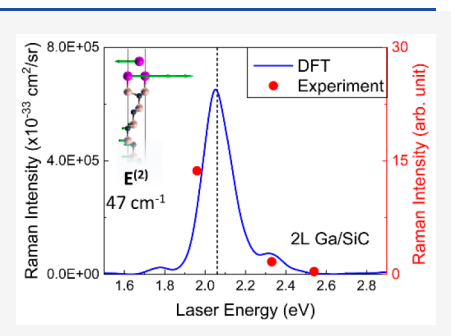
ACCESS I

III Metrics & More

Article Recommendations

SI Supporting Information

ABSTRACT: 2D polar metals synthesized by confinement heteroepitaxy at the SiC/graphene interface are covalently bound to the SiC substrate. In this work, we elucidate the importance of the SiC substrate, and specifically the Ga/Si interface, on the low-frequency resonant Raman spectra of 2D Ga on SiC. The low-frequency Raman modes are dominated by in-plane shear modes in 2D Ga. We show that the frequency of these shear modes is modified by the presence of the substrate for few-layer Ga and that these shear modes couple strongly to the electronic states corresponding to the interface Ga and Si atoms. Consequently, resonant Raman enhancement occurs at laser incident energies that are resonant with the interband optical transitions involving these interface Ga and Si states. This resonant Raman enhancement is observed in laser-energy-dependent measurements, an experimental signature of the strong electron—phonon coupling present in these 2D polar metals.



■ INTRODUCTION

Two-dimensional (2D) polar metals¹ are an emerging class of materials that are covalently bound to semiconductor substrates and yet exhibit quantum confinement as expected for a 2D material system.² These polar metals are synthesized by confinement heteroepitaxy using a silicon carbide (SiC) substrate and are protected by graphene overlayers that form a van der Waals interface with the metals. The polar metals are excellent candidates for functional nanodevices due to their environmental stability, quasi-2D nature, and tunable physical properties. Similar to the more conventional 2D materials, the 2D polar metals exhibit thickness-dependent properties, such as a thickness-dependent dielectric function² and Fermi surface, the latter being important for the emergence of superconductivity.^{1,3}

Low-frequency Raman spectroscopy has proven to be a useful, nondestructive technique to identify the thickness and stacking dependence of 2D semiconducting and semimetallic materials. Using a Green's function approach to take into account the coupling of the 2D metal to the semi-infinite SiC substrate, we have previously predicted that the low-frequency zone-center phonon modes in 2D polar metals are exclusively surface resonance shear modes. Breathing modes are too strongly coupled to the SiC substrate and do not show up as peaks in the phonon density of states. Due to the metallic nature of these systems, it can be challenging to observe these low-frequency shear modes experimentally because of weak nonresonant Raman intensities. It is therefore important to understand the resonant Raman effects in the 2D polar metals in order to guide the design of Raman experiments and to

interpret experimental Raman data. Resonant Raman spectroscopy is also a direct probe of electron—phonon and exciton—phonon coupling effects. The resonant enhancement of Raman scattering in metallic nanoparticles and films arises from plasmons or scattering due to surface states. However, the 2D polar metals are distinct from these metallic systems due to the atomically thin nature of the metals and the strong coupling between the 2D system and the SiC substrate. Because of the strong coupling between the 2D system and the SiC substrate.

The metal—SiC interface in the 2D polar metals is not only critical in the description of vibrational properties of the 2D metal, but also responsible for the optically active interband transitions observed in experimental measurements. In this work, we demonstrate that the metal—SiC interface states play a major role in the resonant enhancement of the low-frequency Raman spectra in the 2D polar metal, Ga. Our calculations show that the peaks in the resonant Raman intensity of the low-frequency shear modes are associated with two physical phenomena. Some peaks arise from the fact that the laser energy is resonant with major interband optical transitions that show up as peaks in the optical absorption spectra, an observation that is consistent with general expectations. However, not all peaks in the resonant Raman intensity

 Received:
 June 26, 2022

 Revised:
 July 28, 2022

 Published:
 August 18, 2022





correspond to peaks in the absorption spectra. We find that other peaks arise due to a particularly pronounced coupling between the shear modes and the interband transitions. Because the shear modes involve a relative movement between the metal atoms and the interface Si atoms, the shear modes can be strongly coupled to the metal—SiC interface states, explaining the significant role of the interface in the resonant Raman enhancement of the shear modes. We also present experimentally measured laser-energy-dependent Raman spectra on 2D Ga that are consistent with the theoretical predictions. Together, the theoretical and experimental studies clearly demonstrate that low-frequency shear modes are observed in 2D Ga, and that these observations are mediated by resonant Raman effects associated with interband transitions involving metal—SiC interface states.

METHODS

Resonant Raman Intensity. Raman signals arise from the inelastic scattering of incident light by the vibrational modes of the system. Within the Placzek approximation, ^{15,16} the intensity of the Raman signal is described by the differential Raman scattering cross-section which is given by ¹⁷

$$\frac{d\sigma_{\mu}}{d\Omega} = \frac{1}{2\hbar^{2}c^{4}E_{\mu}} \frac{(E_{L} - E_{\mu})^{4}}{1 - \exp(-E_{\mu}/k_{B}T)} A_{ij}^{\mu}$$
(1)

where $E_{\rm L}$ and E_{μ} are the energies of the incident light and the phonon mode; \hbar and $k_{\rm B}$ are, respectively, the reduced Planck constant and Boltzmann constant; and A^{μ}_{ij} is the Raman activity of the vibrational mode μ for incident and scattered light polarized in the i and j direction, respectively. Furthermore, $A^{\mu}_{ij} = |\mathcal{R}^{\mu}_{ij}|^2$, where $\mathcal{R}^{\mu}_{ij}(i,j=x,y,z)$ is Raman polarizability tensor. The one-phonon Raman tensor \mathcal{R}^{μ}_{ij} describes the first-order response of the optical polarizability tensor α_{ij} to the phonon eigenmode μ . We use the central difference method to evaluate the Raman tensor, given as

$$\mathcal{R}_{ij}^{\mu}(E_{L}) = \frac{\partial \alpha_{ij}(E_{L})}{\partial \xi^{\mu}}$$

$$\triangleq \frac{1}{\sqrt{M_{0}}} \lim_{s \to 0} \frac{\alpha_{ij}(E_{L})\{R^{0} + s\xi^{\mu}\} - \alpha_{ij}(E_{L})\{R^{0} - s\xi^{\mu}\}}{2s}$$
(2)

where $\xi^{\mu} \equiv \{\xi^{\mu}_{lk}\}$ is the set of atomic displacements corresponding to the phonon eigenmode, μ , of the I^{th} atom along direction k, given as $\xi^{\mu}_{lk} = \frac{u^{\mu}_{lk}}{\sqrt{M_l/M_0}}$, where u^{μ}_{lk} is the eigenvector of mode μ ; M_l is the mass of the I^{th} atom (unit: amu); M_0 is the reference mass which we take to be 1 amu; $R^0 \equiv \{R^0_{lk}\}$ is the set of atomic positions of the system under equilibrium conditions; and s is a scalar. The notation $\frac{\partial}{\partial \xi^{\mu}}$ is defined in eq 2 and used below. Moseler and Walter have reported that the Plazcek approximation agrees qualitatively with the more accurate Albrecht formulation even in the resonant region for the first-order Raman scattering. The energy-dependent polarizability tensor α_{ij} ($E_{\rm L}$) is given in the independent particle approximation as

$$\alpha_{ij}(E_{L}) = \frac{e^{2}}{N_{k}} \sum_{n < n'} \sum_{k} M_{n',n,k}^{ij} \left(\frac{1}{E_{n',k} - E_{n,k} - E_{L} - i\gamma} + \frac{1}{E_{n',k} - E_{n,k} + E_{L} + i\gamma} \right)$$
(3)

This definition gives eventually the Raman intensity corresponding to one surface unit cell, containing one metal atom per layer in the 2D metal system. Here

$$M_{n',n,k}^{ij} = \Lambda_{n',n,k}^{i} \Lambda_{n,n',k}^{j} [f(E_{n,k}) - f(E_{n',k})]$$
(4)

where $\Lambda_{n,n',k}^{\lambda}$ ($\lambda = x, y, \text{ or } z$) is the transition dipole matrix (TDM) element

$$\Lambda_{n,n',k}^{\lambda} = \frac{\hbar}{im_{\rm e}} \frac{\langle n, k | \hat{\mathbf{p}}^{\lambda} | n', k \rangle}{E_{n,k} - E_{n',k}} \tag{5}$$

Here, $|n,k\rangle$ and $|n'k\rangle$ denote the electronic eigenstates with energy $E_{n,k}$ and $E_{n',k}$, respectively; $\hat{\mathbf{p}}^{\lambda}$ is the momentum operator; N_k is the total number of k points sampled in the Brillouin zone (BZ); $m_{\rm e}$ is the electron mass; and $f(E_{n,k})$ is the Fermi–Dirac distribution function, with the temperature taken to be 300 K in this work. The broadening parameter γ is taken to be 0.08 eV. The intraband contributions to the polarizability are neglected here because of their fast decay below 1 eV, ² and our focus on the resonant Raman intensities is from 1 to 3.5 eV.

For further analysis, the Raman tensor \mathcal{R}^{μ}_{ij} can be separated into the double-resonant (DR), single-resonant (SR), and nonresonant (NR) terms, following the nomenclature in refs 19 and 20, which is based on the order of the denominator $(E_{n',k}-E_{n,k}-E_{\rm L}-i\gamma)$ that approaches zero at the resonant condition. These terms are denoted by $\mathcal{R}^{\mu,\nu}_{ij}$ (ν = DR, SR, and NR) and are given by

$$\mathcal{R}_{ij}^{\mu,\nu}(E_{\rm L}) = \sum_{n < n'} \sum_{k} r_{n,n',k}^{\nu} \tag{6}$$

Hence the total Raman intensity is given by

$$\frac{d\sigma_{\mu}}{d\Omega} = \frac{1}{2\hbar^{2}c^{4}E_{\mu}} \frac{(E_{L} - E_{\mu})^{4}}{1 - \exp(-E_{\mu}/k_{B}T)} \left| \sum_{\nu} \mathcal{R}_{ij}^{\mu,\nu}(E_{L}) \right|^{2}$$
(7)

In the text, we also plot Raman intensities arising from each of the DR, SR, and NR terms, computed by using only one of the DR, SR, or NR terms in eq 7.

For simplicity of the notation, the indices ij, μ , and L are omitted in $r^{\nu}_{nn'k}$ for different ν which can be written as

$$r_{n,n',k}^{\mathrm{DR}} = -\frac{e^2}{N_k} \frac{M_{n',n,k}^{ij}}{(E_{n',k} - E_{n,k} - E_{\mathrm{L}} - i\gamma)^2} \frac{\partial (E_{n',k} - E_{n,k})}{\partial \xi^{\mu}}$$
(8)

$$r_{n,n',k}^{\text{SR}} = \frac{e^2}{N_k} \frac{\partial M_{n',n,k}^{ij}}{\partial \xi^{\mu}} \frac{1}{E_{n',k} - E_{n,k} - E_{L} - i\gamma}$$
(9)

and

$$r_{n,n',k}^{NR} = \frac{e^2}{N_k} \frac{\partial}{\partial \xi^{\mu}} \left(\frac{M_{n',n,k}^{ij}}{E_{n',k} - E_{n,k} + E_{L} + i\gamma} \right)$$
(10)

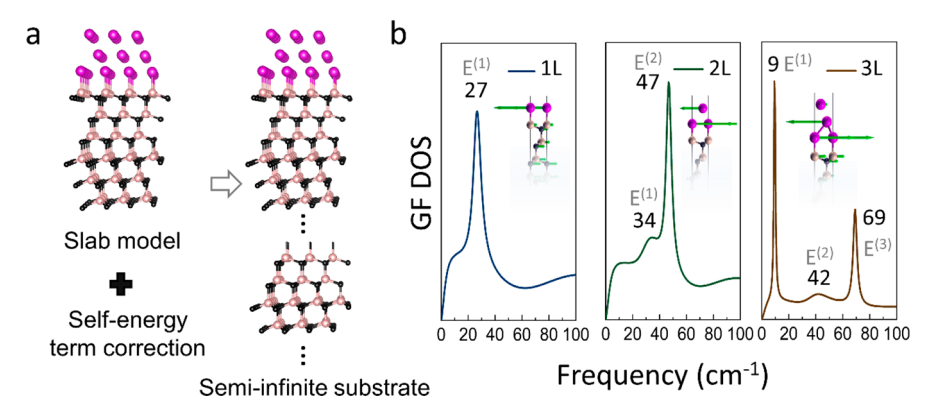


Figure 1. Illustration of Green's function (GF) approach and GF density of states (DOS) at the zone center for 1L to 3L Ga on SiC. (a) Schematic to illustrate the GF approach. Purple, light pink, and black balls refer to Ga, Si, and C atoms, respectively. (b) Computed GF DOS at the zone center for 1L to 3L Ga, obtained with DFT. The insets are atomic displacements (green arrows) of the most prominent mode, $E^{(N)}$, for *N*-layer Ga. Phonon mode frequencies are labeled in cm⁻¹. A top view of the atomic structure is shown in Figure S1.

The DR and SR terms arise from the derivative of the absoprtion term of the polarizability tensor $\alpha_{ij}(E_{\rm L})$ with respect to the phonon displacements, while the NR term arises from the emission term. In eq 8, $\frac{\partial (E_{n',k}-E_{n,k})}{\partial \xi^{\mu}}$ in the DR term is determined by the differences between the diagonal electron–phonon coupling (EPC) matrix elements of the valence and conduction states. The EPC matrix elements for phonon μ at the zone center are defined as 21,22

$$g_{n,n',k}^{\mu} = \sqrt{\frac{\hbar^2}{2M_0 E_{\mu}}} \left\langle n, k \middle| \frac{\partial v^{KS}}{\partial \xi^{\mu}} \middle| n', k \right\rangle$$
(11)

where v^{KS} is the self-consistent Kohn–Sham potential. Diagonal EPC matrix elements can be computed by the changes of the eigen-energy $E_{n,k}$ of the state $|n,k\rangle$ by a phonon displacement via a finite difference approach with central difference

$$g_{n,n,k}^{\mu} = \sqrt{\frac{\hbar^2}{2M_0 E_{\mu}}} \frac{\partial E_{n,k}}{\partial \xi^{\mu}}$$
(12)

First-Principles Calculations. In this work, the atomic structures of few-layer Ga/SiC (Figure 1a) adopt the energetically most stable phases computed by density functional theory (DFT) calculations and are supported by crosssectional scanning transmission electron microscopy (STEM) images. 1,8 The interface Ga atoms sit on top of the Si atoms at the interface and are covalently bonded to these Si atoms. The second and third Ga layers align to the carbon and hollow sites of the interface SiC layer, respectively. In the slab models, the SiC substrate is represented by six layers of SiC passivated by hydrogen atoms, while in the Green's function approach, the SiC substrate is represented as a semi-infinite substrate. Although the polar Ga layers are covered by graphene overlayers in the experiment, these graphene layers do not have a significant impact on the low-frequency phonon modes or the interband optical transitions in the energy range of interest here^{1,3,23} and are not included in the theoretical

DFT calculations are performed using the local density approximation $(LDA)^{24}$ for the exchange-correlation functional as implemented in the plane-wave pseudopotential code, QUANTUM ESPRESSO.²⁵ A plane-wave kinetic energy cutoff of 80 Ry is used, and an energy threshold of 10^{-10} Ry is applied

for the self-consistent cycle. A Monkhorst—Pack k-point mesh of $32 \times 32 \times 1$ is used for geometry optimization, self-consistent field calculations, and density functional perturbation (DFPT) calculations, while a denser k-point mesh of $52 \times 52 \times 1$ is used to get converged Raman scattering intensities. In structural relaxations, all atoms are freely relaxed until the forces acting on each atom are less than 0.0001 Ry/Bohr. To eliminate interactions between slabs, a vacuum length of at least 16 Å with an electrostatic dipole correction is employed. The energy-dependent polarizability tensor is computed using the independent particle approximation. In the sum over states, we include 70 bands involving all valence states to get converged energy-dependent polarizability tensors for 1L to 3L Ga/SiC. For the finite difference method, s in eq 2 is taken to be 0.2 to make sure that the Raman intensities are converged.

Raman Spectra. Raman characterization is performed on a Horiba LabRam HR Evolution system, and all low-frequency measurements were recorded using Volume Bragg Grating notch filters (referred to as ULF filters by Horiba) for each excitation laser. The excitation lasers used for the measurements were 488 nm (Melles Griot 543 series Ar-ion), 532 nm (Oxxious LCX single mode), and 633 nm (ThorLabs HRP-350-EC HeNe) focused through a 100× objective lens (NA 0.9) with a maximum incident laser power of 4 mW. The spectra were recorded with a confocal aperture of 50 μ m, an 1800 gr/mm grating, and a Si-array back-illuminated deepdepleted detector (Horiba-Synapse), which was calibrated using the Raman response of single crystal Si. A baseline offset was applied to the data set, and then spectra were normalized to the folded transverse optical (FTO) mode maximum of the 6H-SiC (789 cm⁻¹).

RESULTS AND DISCUSSION

2D polar metals couple strongly to the SiC substrate via covalent bonding, different from layered van der Waals materials where the coupling with the substrate is much weaker. It is challenging for DFT calculations to accurately capture the influence of a semi-infinite substrate on the vibrational properties of 2D-layered metals, due to the limitation of periodic boundary conditions typically used in such calculations. A first-principles Green's function (GF) approach⁸ was recently implemented to model the effect of a semi-infinite substrate using a self-energy term, as illustrated in Figure 1a. Reference 8 provides details of this approach. The

GF approach revealed that low-frequency zone-center phonons consist of surface resonance shear modes in which in-plane shear motion of the metal layers is coupled to in-plane phonons of the SiC substrate, forming a frequency continuum. Such surface resonance modes show up as peaks with finite width in the GF phonon density of states (DOS) at the zone center⁸ (Figure 1b). This is in contrast to finite slab models with specific thickness-dependent phonon modes at discrete frequencies.8 A broad peak in the GF DOS indicates that the surface resonance phonon mode is strongly coupled to the SiC bulk phonons; in the limit of the semi-infinite substrate, the vibrations of the surface atoms contribute only weakly to the phonon eigenmode. In contrast, a narrow peak indicates the weaker coupling of the surface resonance phonon mode to the substrate, and the phonon eigenmode involves significant displacements in the surface atoms. The GF calculations showed that out-of-plane breathing modes (seen in the finite slab calculations⁸) are so strongly coupled to the SiC substrate that they do not show up as peaks in the GF DOS. Thus, the low-frequency Raman spectra of the 2D polar metals are expected to be dominated by in-plane shear modes. Figure 1b presents the low-frequency GF DOS at the zone center for 1L to 3L Ga on SiC. Besides the ultralow-frequency peak at ~9 cm⁻¹, the predominant peaks in 1L to 3L Ga are the highestfrequency shear mode, which we denote by S1 (E^(N) for Nlayer Ga) (Figure 1b).

In addition to first-principles calculations, it is often useful to employ phenomenological models to understand the physics in the system. In the case of shear modes, linear chain models have been employed to extract the interlayer force constants in various 2D layered materials. 4,27 For the 2D polar metals, we introduce a linear chain model that captures the interaction with a semi-infinite substrate that we model as an infinite mass M (Figure 2a). For 2D Ga specifically, each Ga layer forms a unit in the linear chain, with nearest-neighbor coupling between units. The semi-infinite substrate is also represented as a unit in the linear chain. The in-plane force constants

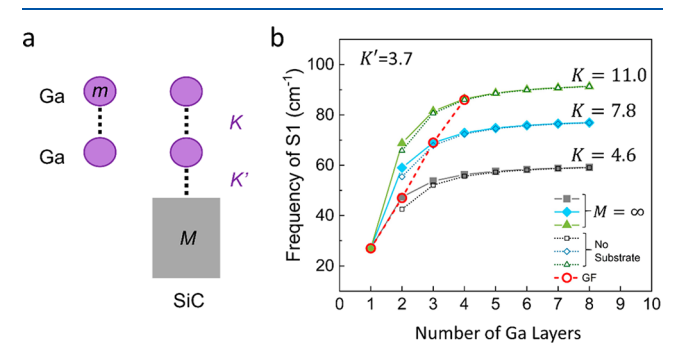


Figure 2. Linear chain models of 2D Ga and the frequencies of mode S1 for 1L-8L Ga. (a) Linear chain models for isolated 2D Ga and 2D Ga coupled to a substrate. The solid circles and gray rectangle denote the Ga layers and SiC substrate, respectively. K and K' (unit: 10^{19} N/m³) are the in-plane shear force constant per unit area between Ga layers and that between the interface Ga layer and SiC, respectively. The mass per area of Ga and the substrate are denoted by m and M in the unit of kg/m², respectively. (b) Frequencies of mode S1 for 1L to 8L Ga/SiC, calculated by using the linear chain model. K and K' are chosen to match the frequencies of S1 computed by the Green's function method (shown in red). K' is 3.7×10^{19} N/m³. The values of K are 4.6, 7.8, and 11.0×10^{19} N/m³ for 2L, 3L, and 4L Ga, respectively.

between Ga layers is denoted as K, and that between the interface Ga layer and the substrate is denoted as K'. Mathematical details of the linear chain model are provided in the Supporting Information. Our first-principles calculations have shown that the low-frequency modes of graphene are decoupled from the phonon modes in the 2D metals,8 and thus, we do not include the graphene layers in our considerations. We use the highest-frequency shear mode S1 to illustrate the results of the linear chain model. Using the case of 1L Ga on the substrate and comparing the results of the linear chain model to that from the DFT GF calculations, we obtain a value of K' to be 3.7×10^{19} N/m³. Observing that the distance between the interface Ga layer and the interface Si layer is essentially the same as the thickness of Ga increases, we make the assumption that K' does not change with the number of Ga layers.

Figure 2b plots the frequency of S1 as a function of the number of Ga layers, N, obtained with the linear chain model using K' of $3.7 \times 10^{19} \text{ N/m}^3$ and different, fixed, values of K. As S1 is an out-of-phase shear mode, the frequency of S1 increases as N increases. However, it can be seen that the linear chain models with fixed K' and K result in a more moderate rate of change of frequency with N compared to the firstprinciples GF approach (shown in red). Evaluating the values of K for N=2, 3, and 4, we see that the effective interlayer force constant K increases from $4.6 \times 10^{19} \text{ N/m}^3$ for N = 2 to $11.0 \times 10^{19} \text{ N/m}^3$ for N = 4. This result is quite unlike those for 2D layered van der Waals materials such as few-layer graphene and transition metal dichalcogenides, for which a single linear chain model with fixed K can reproduce the firstprinciples frequencies.⁴ The increase in K as N increases is, however, consistent with experimental transmission electron microscopy images where the interlayer distance in 2D Ga decreases with N.8 The increasing interlayer force constant with N arises from the asymmetric bonding profile in these polar metals. For example, for N = 2, there are only two Ga layers, and the bottom Ga layer is covalently bonded to Si, which weakens the interlayer bonds within the Ga metal. Finally, we also compare in Figure 2b the results from the linear chain model with no substrate to those with the substrate (solid versus hollow symbols). The presence of the substrate decreases the frequency of S1 for fixed K. This difference is significant for N = 2 and is quite negligible for thicker systems.

Experimental Raman spectra for 2D Ga are found to have some spatial variation over the sample, as indicated by the Raman map analysis in Figure S3. There are two distinct regions with slightly different Raman peak positions, and high signal-to-noise Raman measurements are performed at specific positions in these two regions using incident laser wavelengths of 488, 532, and 633 nm. The results are shown in Figure 3. The Raman intensities are normalized to the FTO mode of 6H-SiC at \sim 789 cm⁻¹ as shown in Figure S2. The broad peaks in the sample reflect the disorder in the sample.²⁸ However, it is evident that there are two major peaks below 100 cm⁻¹ in both regions. The peaks become sharper and more intense as the laser wavelength increases from 488 to 633 nm, i.e., as the laser energy decreases from 2.5 to 2.0 eV. According to these resonant Raman measurements, the peaks have frequencies of \sim 25 cm⁻¹ (R1) and \sim 52 cm⁻¹ (R2) in region A and \sim 28 cm⁻¹ (R1) and ~46 cm⁻¹ (R2) in region B. High-angle annular dark-field cross-sectional scanning transmission electron microscope (HAADF-STEM) images indicate that both regions are

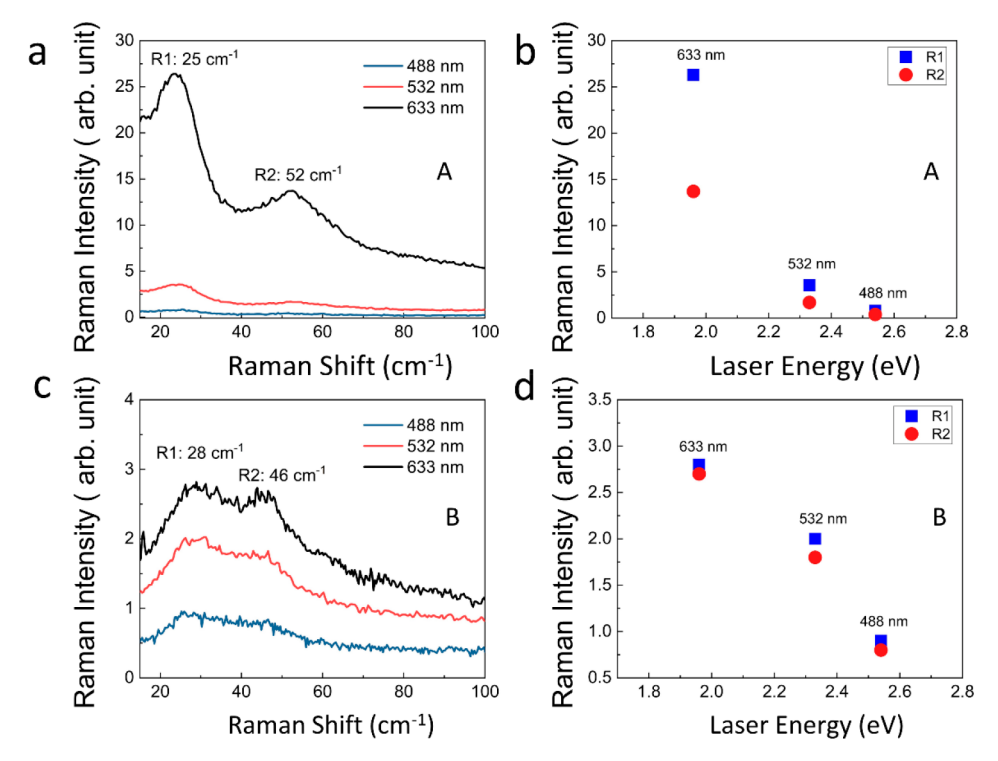


Figure 3. Experimental Raman spectra for 2D Ga in two regions (A and B). (a) and (c) Raman spectra for 2D Ga in regions A and B, respectively, with incident laser wavelengths of 488, 532, and 633 nm. R1 and R2 label the two Raman peaks below 100 cm⁻¹ observed in the experimental Raman spectra (particularly at 633 nm). The Raman spectra are normalized to the FTO mode of 6H-SiC at 789 cm⁻¹ (shown in Figure S2). (b) and (d) Raman intensities of peaks R1 and R2 at different laser energies for region A and region B, respectively.

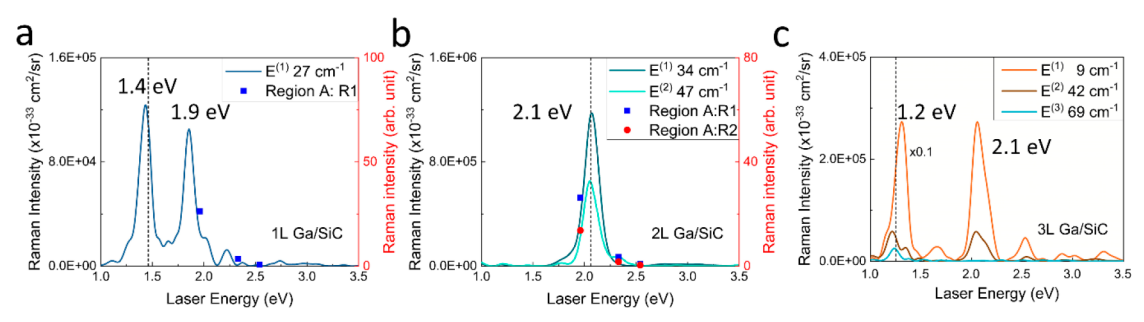


Figure 4. Computed laser-energy-dependent resonant Raman intensities of shear modes of 1-3L Ga. (a) $E^{(1)}$ in 1L Ga/SiC, (b) $E^{(1)}$ and $E^{(2)}$ in 2L Ga/SiC, and (c) $E^{(1)}$, $E^{(2)}$, and $E^{(3)}$ in 3L Ga/SiC. The peak positions for the resonant Raman intensities are labeled. Vertical dashed lines mark the peak positions for the interband optical absorption in these systems (see Figure S4). Experimental Raman results of region A are superposed on computed Raman intensity in (a,b).

dominated by domains of 1L, 2L, and 3L Ga (as shown in Table S1), with region B having a higher proportion of 2L Ga and region A having similar proportions for 1L, 2L, and 3L Ga. The Auger mapping in Figure S3c suggests that region A has more Ga, a finding that is overall consistent with the HAADF-STEM results (Table S1).

According to the symmetry of 2D Ga, the Raman tensors of double-degenerate shear modes, E(x) and E(y) (labeled by the irreducible representation E), are given by

$$\mathcal{R}[E(x)] = \begin{bmatrix} 0 & a & b \\ a & 0 & 0 \\ b & 0 & 0 \end{bmatrix} \quad \text{and} \quad \mathcal{R}[E(y)] = \begin{bmatrix} a & 0 & 0 \\ 0 & -a & b \\ 0 & b & 0 \end{bmatrix}$$

The Raman intensity is proportional to $|e_i \cdot \mathcal{R} \cdot e_s|^2$, where e_i and e_s are the polarization vectors of the incident light and scattered light, respectively. Figure 4 shows the computed resonant

Raman intensities for the zone center shear modes for 1L to 3L Ga ($|a|^2$ for each mode) for incident laser energies of 1.0–3.5 eV. Here, finite slabs with six SiC layers are used to compute the resonant Raman intensities (see Methods). The dashed lines mark the peak positions for the interband optical transitions (see also Figure S4 for the computed optical absorption spectra). In all the systems, we see that the peak positions in the optical absorption spectra also correspond to peaks in the resonant Raman intensities for the shear modes. However, there are additional peaks in the resonant Raman spectra at laser energies that are different from the peak positions in the optical spectra.

Focusing on the trend in the Raman intensities as a function of laser energies (2.0–2.5 eV in the experiment), the computed resonant Raman spectra suggest that possible origins of the experimentally observed peaks are $E^{(1)}$ in 1L Ga, $E^{(1)}$ and $E^{(2)}$ in 2L Ga, and $E^{(2)}$ in 3L Ga. (The \sim 9 cm⁻¹ frequency of $E^{(1)}$ in

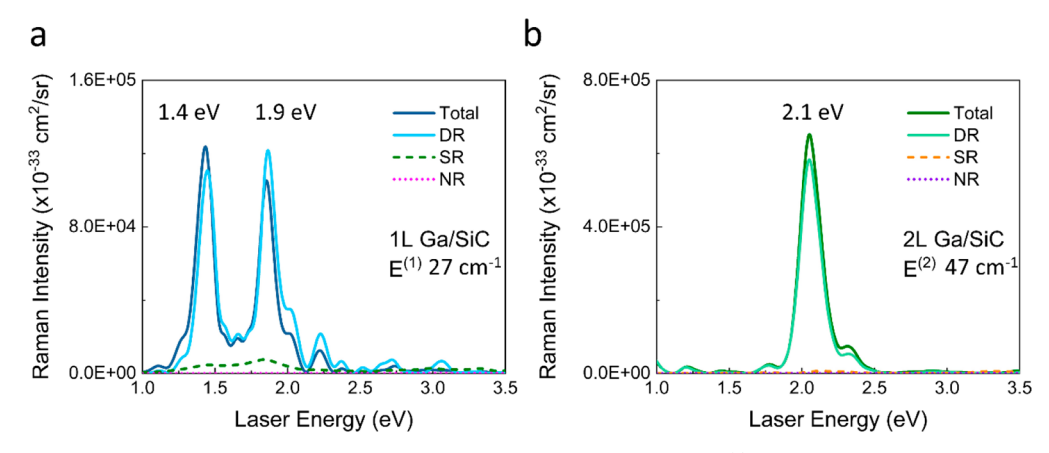


Figure 5. Computed laser-energy-dependent resonant Raman intensities of shear modes. (a) $E^{(1)}$ in 1L Ga/SiC at 27 cm⁻¹ and (b) $E^{(2)}$ in 2L Ga/SiC at 47 cm⁻¹. The atomic displacements of the two modes are illustrated in Figure 1b. Raman intensities computed from the DR, SR, and NR components of the Raman tensors are indicated by solid, dashed, and dotted lines, respectively. A similar analysis for other phonon modes in 2L and 3L Ga can be found in Figure S5.

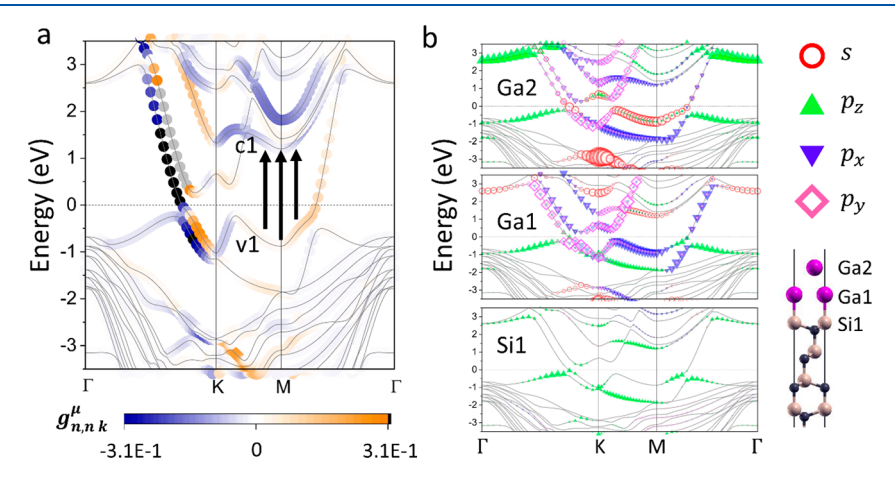


Figure 6. Analysis of the origin of resonant Raman intensities for the $E^{(2)}$ mode of 2L Ga/SiC. (a) Diagonal electron—phonon coupling matrix elements $g_{n,n,k}^{\mu}$ of the mode $E^{(2)}$ in 2L Ga/SiC, given in units of eV, overlain on the electronic band structure. Black arrows depict schematically the transitions at 2.1 eV (Figure S4). (b) Electronic band structure with projections of wave functions on orbitals of Ga2, Ga1, and Si1 atoms (see inset), as indicated by the sizes of the colored symbols.

3L Ga is beyond the detectable spectral range in experiment.) At the same time, bearing in mind that the resonant Raman calculations were performed on finite slabs, we also refer to Figure 1b, which gives the GF phonon DOS at the zone center. Figure 1b indicates that, at the zone center, $E^{(1)}$ in 2L Ga and E(2) in 3L Ga are both strongly coupled to SiC, and that in the limit of a semi-infinite substrate the contribution of Ga displacements to these coupled modes is small. We therefore expect that the zone-center phonons giving rise to large resonant Raman intensities at ~2.0 eV correspond to S1 modes in 1L and 2L Ga, which were predicted to be at \sim 27 cm⁻¹ and ~47 cm⁻¹, respectively, in reasonable agreement with the experimentally measured frequencies and trends in the laser-energy-dependent resonant Raman intensities (Figure 4a,b). In ref 8, we had also discussed the possibility of scattering from phonons away from the zone center, arising from disorder in the sample, which would be especially relevant for alloy samples. In particular, the phonon branch corresponding to $E^{(1)}$ in 2L Ga (~34 cm⁻¹ at the zone center) decouples from the bulk SiC phonon band at finite momenta, where phonons become more localized on Ga.8 Noting the large resonant Raman intensity predicted for E⁽¹⁾ in 2L Ga at ~2.0 eV incident laser energy (an order of magnitude larger

than that for $E^{(1)}$ in 1L Ga), it is conceivable that $E^{(1)}$ in 2L Ga may also contribute to the R1 peak in the presence of disorder or domains. We note that S1 ($E^{(3)}$) in 3L Ga has a much weaker resonant Raman intensity at ~2.0 eV laser energy than the other shear modes considered here. This weak intensity explains the absence of a peak at ~69 cm⁻¹ (the frequency of $E^{(3)}$) in the experimental Raman spectra in Figure 3, despite the relatively sharp peak for $E^{(3)}$ in the GF DOS in Figure 1b. The slight differences between the experimental Raman spectra for regions A and B are likely due to differences in the scattering length and domain sizes in these regions. While our theoretical predictions for the idealized 1L to 3L Ga systems do not explain in detail the differences between the two regions, they do show clearly that the Raman peaks in the experimental spectra can be attributed to shear modes in 2D Ga

In order to elucidate the origins of the resonant Raman enhancement, we plot in Figure 5 the total Raman intensity, as well as the Raman intensities obtained from individual components of the Raman tensor (the double-resonant (DR), single-resonant (SR), and nonresonant (NR) terms; eqs 6-10) for the S1 modes in 1L and 2L Ga. From Figure 5, it is clear that the DR term is dominant. The DR term is also

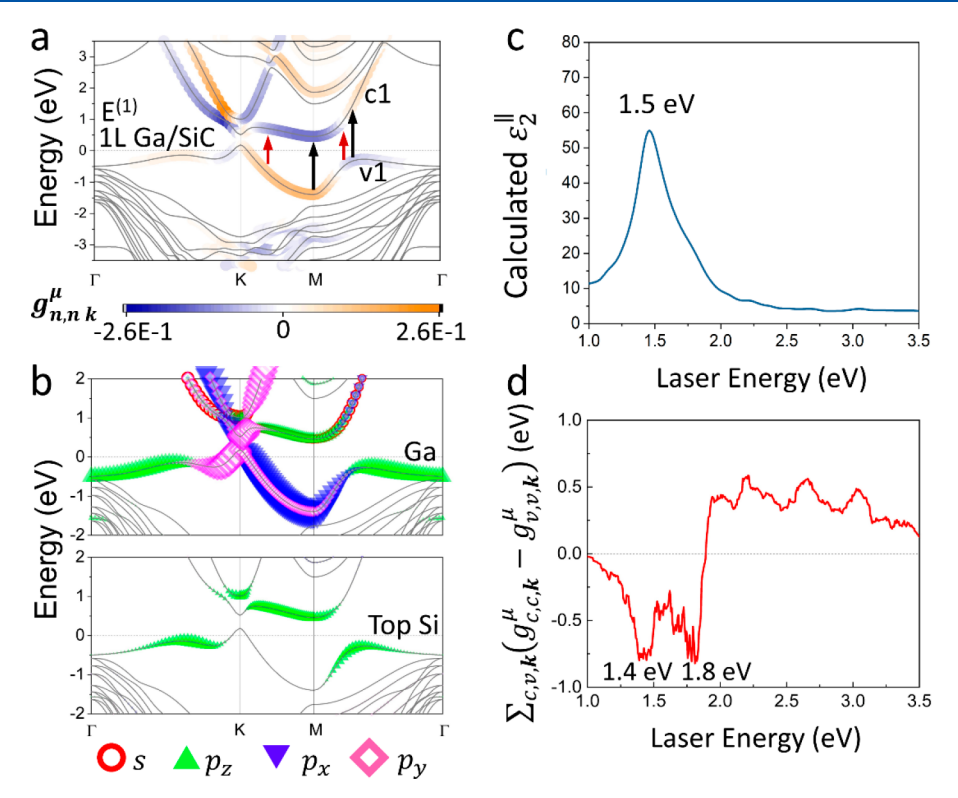


Figure 7. Analysis of the origin of resonant Raman intensities for the $E^{(1)}$ mode of 1L Ga/SiC. (a) Diagonal electron—phonon coupling matrix elements $g_{n,n,k}^{\mu}$ of the mode $E^{(1)}$ in 1L Ga/SiC, given in units of eV, overlain on the electronic band structure. Arrows depict schematically the transitions at 1.4 eV (red) and 1.9 eV (black), as analyzed in Figure S6. (b) Electronic band structure with projections of wave functions on orbitals of Ga (top) and top Si (bottom) atoms, as indicated by the sizes of the colored symbols. (c) Calculated imaginary part of the dielectric function, $\varepsilon_2^{\parallel}$ ($\varepsilon_2^{\parallel} = \varepsilon_2^{xx} = \varepsilon_2^{yy}$), for 1L Ga/SiC with in-plane parallel polarizations. (d) Summation of $(g_{c,c,k}^{\mu} - g_{v,v,k}^{\mu})$ over the Brilliouin zone and states c and v, i.e., $\sum_{c,v,k} (g_{c,c,k}^{\mu} - g_{v,v,k}^{\mu})$, for transitions which have more than 0.2% contribution to $\varepsilon_2^{\parallel}$ at each laser energy. In the summation, a Lorentzian broadening is applied with a broadening factor of 0.08 eV (same as that used to plot $\varepsilon_2^{\parallel}$).

dominant for the other shear modes in 1L to 3L Ga (Figure S5). For the \mathcal{R}_{xx} component, the DR term is given by

$$\mathcal{R}_{xx}^{\mu,DR}(E_{L}) = -\frac{e^{2}}{N_{k}} \sqrt{\frac{2M_{0}E_{\mu}}{\hbar^{2}}}$$

$$\sum_{\nu,c} \sum_{k} \frac{M_{\nu,c,k}^{xx}}{(E_{c,k} - E_{\nu,k} - E_{L} - i\gamma)^{2}}$$

$$(g_{c,c,k}^{\mu} - g_{\nu,\nu,k}^{\mu})$$
(13)

Here, $M_{\nu,c,k}^{xx}$ is the square of the norm of the transition dipole matrix elements, multiplied by a factor involving the occupation number (eqs 4 and 5), and $g_{c,c,k}^{\mu}$ and $g_{v,v,k}^{\mu}$ are diagonal electron-phonon coupling matrix elements of the conduction state c and valence state v at k for mode μ (eq 12). The definitions of other quantities can be found in the Methods section. Physically, the DR term corresponds to processes in which the electron scatters with a phonon within the same band; i.e., this process involves electron-phonon matrix coupling terms that are diagonal in the basis of electronic states $(g_{n,n,k}^{\mu})$. The "double-resonant" nomenclature refers to the denominator in the DR term involving $(E_{c,k} - E_{\nu,k})$ $-E_{\rm L}-i\gamma)^2$, where $E_{c,k}$ and $E_{v,k}$ are the eigenenergies of state c and ν ; $E_{\rm L}$ is the laser energy; and γ is a broadening factor. Both the incident and scattered light are resonant with the interband transition.

It is typically expected that the resonant Raman intensity as a function of incident laser energy will peak at the same energy as the optical absorption peaks. Mathematically, this correspondence can be understood from the transition dipole matrix elements in the numerator of the DR term (eq 13) as well as the energy denominator. Both 1L and 2L Ga have prominent peaks in the imaginary part of the dielectric function, corresponding to optical absorption. The peaks (1.5 eV for 1L Ga and 2.1 eV for 2L Ga² (Figure S4)) correspond to interband transitions from an occupied Ga state to an unoccupied state involving the metal and interface Si layer. We illustrate in Figure 6a (arrows) the interband transition corresponding to 2.1 eV in 2L Ga-a transition that is particularly relevant for the chosen laser energies in the experiment. From Figure 6b, it is clear that these states involve the interface Si states as well as the Ga states. A detailed discussion of the states involved in the optical transition is given in ref 2.

Resonant Raman enhancement involving interband transitions is an important experimental signature of electron—phonon coupling in the system. As shown in eq 13, the term, $(g_{c,c,k}^{\mu} - g_{v,v,k}^{\mu})$, is important for the DR term. This is the difference between the diagonal electron—phonon coupling matrix element for the conduction state and that for the valence state. Figure 6b illustrates, for the $E^{(2)}$ phonon mode in 2L Ga, the diagonal electron—phonon coupling matrix elements overlain on the electronic band structure. Importantly, the signs of the electron—phonon matrix elements are different for the conduction and valence states involved in the interband transitions indicated by the arrows, leading to a large value of $(g_{c,c,k}^{\mu} - g_{v,v,k}^{\mu})$, thus leading to a significant resonant

enhancement of the Raman intensities of the shear mode. Similar observations can be made for the $E^{(1)}$ mode in 2L Ga (Figure S7).

For the 1L case, the transition at 1.4 eV (Figure 7c) is schematically illustrated by red arrows in Figure 7a, and the orbital-projected electronic band structure is shown in Figure 7b. Similar to the 2L case, interband transitions involving the Si and Ga interface states are critical in the resonant Raman enhancement of the shear modes. The electron—phonon coupling matrix elements for the Ga states and interface Si states have large magnitudes (Figure 7a,b), consistent with the phonon eigenmode which involves the motion of Ga atoms relative to the interface Si layer. The signs of the electron—phonon matrix elements are also different for the conduction and valence states involved in the interband transitions indicated by the arrows, leading to a large value of $(g^{\mu}_{c,c,k} - g^{\mu}_{\nu,\nu,k})$.

In Figure 4, we showed that the resonant Raman spectra as a function of incident laser energy can peak at additional energies at which there is no prominent optical absorption peak. This observation is relevant to interpret the resonant Raman enhancement for E⁽¹⁾ in 1L Ga at 1.9 eV. To understand this phenomenon, we plot $\sum_{c,v,k} (g^{\mu}_{c,c,k} - g^{\mu}_{v,v,k})$ as a function of incident laser energy in Figure 7d. It can be observed that the magnitude of this quantity peaks at 1.8 eV, very close to the additional peak in the resonant Raman intensity for $E^{(1)}$ in 1L Ga (1.9 eV). The quantity also peaks at 1.4 eV, which corresponds to the peak in the optical absorption spectra. Taken together, this analysis shows that resonant Raman effects are accentuated at incident laser energies corresponding to peaks in $\sum_{c,v,k} (g^{\mu}_{c,c,k} - g^{\mu}_{v,v,k})$, as well as peaks at the optical absorption spectra as long as electron—phonon coupling effects are significant and of the opposite sign for the unoccupied and occupied electronic states. Further analysis on the peak at 2.1 eV for E⁽²⁾ of 3L Ga is shown in Figure S8, with similar conclusions.

In previous work, we had shown that the graphene overlayer does not affect the optical transitions in the range of 1.0–3.0 eV in the metal/SiC systems. Our computed optical absorption energies without graphene are in good agreement with ellipsometry measurements.^{2,3} However, the graphene overlayer changes the Fermi level of the system, and the experimental Fermi level for 2L Ga is 0.6 eV higher than the computed Fermi level without graphene.¹ In Figure S9 we show that the resonant Raman intensities do not change significantly with small shifts in the Fermi level up to 0.6 eV, for the shear modes that are of interest in this work.

CONCLUSIONS

In summary, we have demonstrated that strong light—matter interactions and electron—phonon coupling between the shear modes and the metal/Si interface states lead to significant resonant Raman enhancement effects in a monoelement 2D polar metal—2D Ga on SiC. This observation demonstrates that the SiC substrate not only supports the growth of the 2D metal but also plays an important role in the electronic, vibrational, and optical properties of the 2D polar metals. The laser-energy-dependent Raman spectra are a clear experimental demonstration of the strong electron—phonon coupling present in 2D Ga on SiC. An understanding of the electron—phonon coupling in these novel 2D polar metals has important implications for their applications in advanced technologies, such as superconductors.

ASSOCIATED CONTENT

Supporting Information

The Supporting Information is available free of charge at https://pubs.acs.org/doi/10.1021/acs.jpcc.2c04433.

Top view of atomic structure, details of the linear chain model, experimental Raman spectra for 2D Ga in a larger frequency range (<1000 cm⁻¹), Raman mapping of the 2D Ga sample, the imaginary part of in-plane dielectric functions $\varepsilon_2^{\parallel}$ ($\varepsilon_2^{\parallel} = \varepsilon_2^{xx} = \varepsilon_2^{yy}$) for 1–3L Ga, statistical analysis of the thickness of Ga from cross-sectional HAADF-STEM images, computed laser-energy-dependent resonant Raman intensities of other shear modes, k-resolved imaginary part of dielectric function ε_2^{yy} of 1L Ga, analysis of the electron—phonon couplings for E⁽¹⁾ of 2L Ga/SiC, analysis of the electron—phonon couplings for E⁽²⁾ of 3L Ga/SiC, and computed laser-energy-dependent resonant Raman intensities of surface resonance modes with a Fermi level shift (PDF)

AUTHOR INFORMATION

Corresponding Author

Su Ying Quek — Department of Physics, National University of Singapore, Singapore 117551, Singapore; Centre for Advanced 2D Materials, National University of Singapore, Singapore 117546, Singapore; Department of Materials Science and Engineering, National University of Singapore, Singapore 117575, Singapore; NUS Graduate School Integrative Sciences and Engineering Programme, National University of Singapore, Singapore 117456, Singapore; orcid.org/0000-0003-4223-2953; Email: phyqsy@nus.edu.sg

Authors

Wen He — Department of Materials Science and Engineering, National University of Singapore, Singapore 117575, Singapore; Centre for Advanced 2D Materials, National University of Singapore, Singapore 117546, Singapore; Present Address: Department of Physics, National University of Singapore, 2 Science Drive 3, Singapore 117551, Singapore; Orcid.org/0000-0001-7972-8667

Maxwell T. Wetherington — Department of Materials Science and Engineering, The Pennsylvania State, University Park, Pennsylvania 16802, United States; Materials Research Institute, The Pennsylvania State University, University Park, Pennsylvania 16802, United States; ◎ orcid.org/0000-0003-1958-1354

Kanchan Ajit Ulman — Centre for Advanced 2D Materials, National University of Singapore, Singapore 117546, Singapore; Department of Physics, National University of Singapore, Singapore 117551, Singapore; orcid.org/0000-0002-5434-6563

Joshua A. Robinson — Department of Materials Science and Engineering, The Pennsylvania State, University Park, Pennsylvania 16802, United States; Materials Research Institute, Center for 2-Dimensional and Layered Materials, and 2-Dimensional Crystal Consortium, The Pennsylvania State University, University Park, Pennsylvania 16802, United States; Occid.org/0000-0002-1513-7187

Complete contact information is available at: https://pubs.acs.org/10.1021/acs.jpcc.2c04433

Notes

The authors declare no competing financial interest.

ACKNOWLEDGMENTS

W.H., K.A.U., and S.Y.Q. acknowledge funding from Grants MOE2016-T2-2-132, MOE2017-T2-2-139, and MOE2018-T3-1-005 from the Ministry of Education (MOE), Singapore, funding from the MOE Research Scholarship Block, and funding from the Singapore National Research Foundation, Prime Minister's Office, under its medium-sized center program. Computations were performed on the NUS Graphene Research Centre cluster and National Supercomputing Centre Singapore (NSCC). J.A.R. and M.T.W. are supported in part by Horiba and the Penn State Center for Nanoscale Science through the National Science Foundation Grant DMR-2011839. All Raman measurements were performed in the Materials Research Institute at the Materials Characterization Laboratory at Penn State University.

REFERENCES

- (1) Briggs, N.; Bersch, B.; Wang, Y.; Jiang, J.; Koch, R. J.; Nayir, N.; Wang, K.; Kolmer, M.; Ko, W.; De La Fuente Duran, A.; et al. Atomically Thin Half-van Der Waals Metals Enabled by Confinement Heteroepitaxy. *Nat. Mater.* **2020**, *19* (6), 637–643.
- (2) Nisi, K.; Subramanian, S.; He, W.; Ulman, K. A.; El-Sherif, H.; Sigger, F.; Lassaunière, M.; Wetherington, M. T.; Briggs, N.; Gray, J.; et al. Light-matter Interaction in Quantum Confined 2D Polar Metals. *Adv. Funct. Mater.* **2020**, 2005977.
- (3) Rajabpour, S.; Vera, A.; He, W.; Katz, B. N.; Koch, R. J.; Lassaunière, M.; Chen, X.; Li, C.; Nisi, K.; El-Sherif, H.; et al. Tunable 2D Group-III Metal Alloys. *Adv. Mater.* **2021**, 33, 2104265.
- (4) Zhao, Y.; Luo, X.; Li, H.; Zhang, J.; Araujo, P. T.; Gan, C. K.; Wu, J.; Zhang, H.; Quek, S. Y.; Dresselhaus, M. S.; et al. Interlayer Breathing and Shear Modes in Few-trilayer MoS₂ and WSe₂. *Nano Lett.* **2013**, *13* (3), 1007–1015.
- (5) Puretzky, A. A.; Liang, L.; Li, X.; Xiao, K.; Wang, K.; Mahjouri-Samani, M.; Basile, L.; Idrobo, J. C.; Sumpter, B. G.; Meunier, V.; et al. Low-frequency Raman Fingerprints of Two-dimensional Metal Dichalcogenide Layer Stacking Configurations. *ACS Nano* **2015**, 9 (6), 6333–6342.
- (6) Ferrari, A. C.; Meyer, J. C.; Scardaci, V.; Casiraghi, C.; Lazzeri, M.; Mauri, F.; Piscanec, S.; Jiang, D.; Novoselov, K. S.; Roth, S.; et al. Raman Spectrum of Graphene and Graphene Layers. *Phys. Rev. Lett.* **2006**, *97* (18), 187401.
- (7) Lin, M.-L.; Chen, T.; Lu, W.; Tan, Q.-H.; Zhao, P.; Wang, H.-T.; Xu, Y.; Tan, P.-H. Identifying the Stacking Order of Multilayer Graphene Grown by Chemical Vapor Deposition via Raman Spectroscopy. *J. Raman Spectrosc.* **2018**, 49 (1), 46–53.
- (8) He, W.; Wetherington, M. T.; Ulman, K. A.; Gray, J. L.; Robinson, J. A.; Quek, S. Y. Shear Modes in a 2D Polar Metal. *J. Phys. Chem. Lett.* **2022**, *13* (18), 4015–4020.
- (9) Mills, D. L.; Maradudin, A. A.; Burstein, E. Theory of the Raman Effect in Metals. *Ann. Phys.* (N. Y.) 1970, 56 (2), 504–555.
- (10) Carvalho, B. R.; Malard, L. M.; Alves, J. M.; Fantini, C.; Pimenta, M. A. Symmetry-dependent Exciton-Phonon Coupling in 2D and Bulk MoS₂ Observed by Resonance Raman Scattering. *Phys. Rev. Lett.* **2015**, *114* (13), 136403.
- (11) Portales, H.; Saviot, L.; Duval, E.; Fujii, M.; Hayashi, S.; Del Fatti, N.; Vallée, F. Resonant Raman Scattering by Breathing Modes of Metal Nanoparticles. *J. Chem. Phys.* **2001**, *115* (8), 3444–3447.
- (12) Portalès, H.; Goubet, N.; Saviot, L.; Yang, P.; Sirotkin, S.; Duval, E.; Mermet, A.; Pileni, M.-P. Crystallinity Dependence of the Plasmon Resonant Raman Scattering by Anisotropic Gold Nanocrystals. *ACS Nano* **2010**, *4* (6), 3489–3497.
- (13) Akemann, W.; Otto, A.; Schober, H. R. Raman Scattering by Bulk Phonons in Microcrystalline Silver and Copper via Electronic Surface Excitations. *Phys. Rev. Lett.* **1997**, *79* (25), 5050–5053.

- (14) del Corro, E.; Terrones, H.; Elias, A.; Fantini, C.; Feng, S.; Nguyen, M. A.; Mallouk, T. E.; Terrones, M.; Pimenta, M. A. Excited Excitonic States in 1L, 2L, 3L, and Bulk WSe₂ Observed by Resonant Raman Spectroscopy. *ACS Nano* **2014**, 8 (9), 9629–9635.
- (15) Placzek, G. The Rayleigh and Raman Scattering; Lawrence Radiation Laboratory: CA, 1959.
- (16) Profeta, M.; Mauri, F. Theory of Resonant Raman Scattering of Tetrahedral Amorphous Carbon. *Phys. Rev. B* **2001**, *63* (24), 245415. (17) Murphy, W. F.; Holzer, W.; Bernstein, H. J. Gas Phase Raman Intensities: A Review of "Pre-Laser" Data. *Appl. Spectrosc.* **1969**, 23 (3), 211–218.
- (18) Walter, M.; Moseler, M. Ab Initio Wavelength-Dependent Raman Spectra: Placzek Approximation and Beyond. *J. Chem. Theory Comput.* **2020**, *16* (1), 576–586.
- (19) Miranda, H. P.; Reichardt, S.; Froehlicher, G.; Molina-Sánchez, A.; Berciaud, S.; Wirtz, L. Quantum Interference Effects in Resonant Raman Spectroscopy of Single- and Triple-layer MoTe₂ from First-principles. *Nano Lett.* **2017**, *17* (4), 2381–2388.
- (20) Pereira Coutada Miranda, H. Ab initio Approaches to Resonant Raman Spectroscopy of Transition Metal Dichalcogenides. *Ph.D. Dissertation*, University of Luxembourg, Luxembourg, Luxembourg, 2017. https://orbilu.uni.lu/handle/10993/32659 (accessed 2017-09-22).
- (21) Giustino, F. Electron-phonon Interactions from First Principles. *Rev. Mod. Phys.* **2017**, *89* (1), 015003.
- (22) Giustino, F.; Cohen, M. L.; Louie, S. G. Electron-phonon Interaction Using Wannier Functions. *Phys. Rev. B* **2007**, *76* (16), 165108.
- (23) Wetherington, M. T.; Turker, F.; Bowen, T.; Vera, A.; Rajabpour, S.; Briggs, N.; Subramanian, S.; Maloney, A.; Robinson, J. A. 2-dimensional Polar Metals: A Low-frequency Raman Scattering Study. 2d Mater. 2021, 8 (4), 041003.
- (24) Perdew, J. P.; Wang, Y. Accurate and Simple Analytic Representation of the Electron-gas Correlation Energy. *Phys. Rev. B* **1992**, 45 (23), 13244–13249.
- (25) Giannozzi, P.; Baroni, S.; Bonini, N.; Calandra, M.; Car, R.; Cavazzoni, C.; Ceresoli, D.; Chiarotti, G. L.; Cococcioni, M.; Dabo, I.; et al. QUANTUM ESPRESSO: A Modular and Open-source Software Project for Quantum Simulations of Materials. *J. Condens. Matter Phys.* **2009**, *21* (39), 395502.
- (26) Yu, P. Y.; Cardona, M. Fundamentals of Semiconductors: Physics and Materials Properties; Springer: Heidelberg, Dordrecht, London, NY, 2010.
- (27) Zhao, Y.; Luo, X.; Zhang, J.; Wu, J.; Bai, X.; Wang, M.; Jia, J.; Peng, H.; Liu, Z.; Quek, S. Y.; Xiong, Q. Interlayer Vibrational Modes in Few-quintuple-layer Bi₂Te₃ and Bi₂Se₃ Two-dimensional Crystals: Raman Spectroscopy and First-principles Studies. *Phys. Rev. B* **2014**, 90 (24), 245428.
- (28) Richter, H.; Wang, Z. P.; Ley, L. The One Phonon Raman Spectrum in Microcrystalline Silicon. *Solid State Commun.* **1981**, 39 (5), 625–629.